IEEE Access
Multidisciplinary | Rapid Review | Open Access Journal

Received August 29, 2020, accepted September 8, 2020, date of publication September 18, 2020, date of current version October 1, 2020.

Digital Object Identifier 10.1109/ACCESS.2020.3024935

Duty-Cycle Predictive Control of Quasi-Z-Source Modular Cascaded Converter Based Photovoltaic Power System

YINGJUN GUO[1,2], HEXU SUN[1,2], (Senior Member, IEEE), YI ZHANG[1,2], YUSHAN LIU[3], (Senior Member, IEEE), XIAO LI[4], (Member, IEEE), AND YAOSUO XUE[5], (Senior Member, IEEE)

[1]School of Electrical Engineering, Hebei University of Science and Technology, Shijiazhuang 050018, China
[2]School of Artificial Intelligence, Hebei University of Technology, Tianjin 300130, China
[3]School of Automation Science and Electrical Engineering, Beihang University, Beijing 100083, China
[4]Department of Electrical and Computer Engineering, Texas A&M University, College Station, TX 77843, USA
[5]Oak Ridge National Laboratory, Oak Ridge, TN 37831, USA

Corresponding authors: Hexu Sun (sun@backslashprof@163.com) and Xiao Li (xiaoli.tamu@gmail.com)

This work was supported in part by the Science and Technology Support Project of Hebei Province under Grant 19214501D, in part by the Funding Project by Hebei Foreign Experts Affairs Bureau under Grant 2019YX005A, and in part by the Fundamental Research Funds for the Central Universities, under Grant KG16034501, China.

ABSTRACT A duty-cycle predictive control is proposed for dc grid integration of front-end isolated quasi-Z-source modular cascaded converter (qZS-MCC) photovoltaic (PV) power system. The post-stage qZS half-bridge dc-dc converter deals with PV maximum power point tracking, dc grid integration, and dc-link voltage balance; whereas, the front-end isolation converters operate at a constant duty cycle of 50%. Thus, it saves control hardware resources while overcoming challenges from PV-panel voltage variations and dc-bus voltage limit. The proposed control uses the derived circuit model to predict the global active-state duty cycle for grid-connected current control and predict the shoot-through duty cycles for dc-link voltage balance, achieving a fast and accurate tracking target. The proposed control method has advantages of: i) eliminating weighting factors that exist in conventional model predictive control (MPC), ii) no sophisticated loop parameters design that exists in proportional-integral (PI) control, iii) operating at constant switching frequency that is different from the conventional MPC with variable switching frequency. Simulation and experimental tests are carried out to verify the effectiveness of the proposed control method and compare with the PI-based control system.

INDEX TERMS Photovoltaic power system, dc-dc power conversion, quasi-Z-source converter, predictive control.

I. INTRODUCTION

Nowadays, the ever-increasing installed capacity of the large-scale photovoltaic (PV) power plants locate in remote areas, which usually have abundant irradiation. Therefore, accommodating high voltage (HV) dc transmission can lower power loss [1]. Conventional solutions commonly use a central inverter with a bulky step-up transformer or the cascaded multilevel inverter, in order to invert the dc voltage from the PV panels into a HV ac bus [2]–[4]. The high ac voltage is then converted to a high dc voltage for the long-distance transmission. A decoupling inverter is further required to recover the ac voltage from the high dc voltage, to match the utility grid or load. Such multistage conversion, i.e., dc-ac-HV ac-HV dc-ac, encounters challenges of cost, efficiency, and power density [5].

Considering the natural dc characteristics of PV power, motivations have been concentrated toward dc collection of PV power at the distribution level, forming the configuration of dc-HV dc-ac [6]–[8]. Due to the limit on insulation voltage of commercial PV panels which is normally 1.5 kV, galvanic isolation is normally required to protect the PV panels. For those purposes, the quasi-Z-source modular cascaded converter (qZS-MCC) with dc integration of PV power is proposed in [7]–[12]. The qZS-MCC is formed by front-end isolated qZS half-bridge (HB) PV submodules (SMs), which isolates the PV panels from HV side of qZS-MCC. Thus, it overcomes the insulation voltage limit

The associate editor coordinating the review of this manuscript and approving it for publication was Firuz Zare.

of PV panels. With cascaded structure on the dc output of qZS-HB SMs, a high dc-bus voltage is directly obtained. It is workable to extend the operation power scale with multi qZS-MCC PV systems parallelly tied to the dc collection grid to expand the power simply at utility scale. In addition, inherited from the characteristics of quasi-Z-source inverter (qZSI) [13]–[18], the post-stage qZS-HB dc-dc converter is able to deal with PV maximum power point tracking (MPPT) and dc-link voltages balance. Hence, only a unified and constant 50% duty cycle is applied to the front-end isolation converters of all SMs, without any extra control efforts needed. Therefore, hardware resources and costs can be significantly saved, especially in cases with numbers of SMs, compared to its counterparts which are consisted of two-stage isolated dc-dc converters [19]–[21].

System-level control method of the qZS-MCC PV power system has been developed, using $2n+1$ proportional-integral (PI) control loops for n SMs formed qZS-MCC [10], [12]. In the previous work, each SM needs a dual-loop PI regulator-based shoot-through (ST) duty cycle control to balance the dc-link voltages, and one extra PI regulator-based PV panel voltage control to track the MPPT, while a PI regulator controlling the dc grid-connected current. Whereas, design of PI-based control is a tough task, especially for multi-loop PI controls, because sophisticated controller parameters design based on system transfer functions and Bode plots is usually needed, to play with tradeoff between stability and transient optimization [22]–[26]. In addition, stability and rapidity of the PV power system are highly dependent on PI parameters. Derivative regulator could be combined to improve the performance, but it also increases the design complexity [27].

Various contributions have been dedicated to the control of traditional qZSI power systems. To improve the dynamic responses with respect to PI-based control, the non-linear fuzzy logic control [28], neural network control [29], sliding mode control (SMC) [30]–[33], and model predictive control (MPC) [34]–[39] were developed. Among them, the SMC and MPC were paid high attractions due to the simple implementation through digital controllers [40], [41]. Besides that, the MPC has accurate tracking capability to the reference, fast dynamic responses to condition changes, and is insensitive to circuit parameters variations. The conventional MPC predicts the qZS-network capacitor voltage and inductor current, as well as output current for the next control cycle; then evaluates the defined cost function at all the switching states in the present control cycle; the one corresponding with the minimum value of cost function is selected as the switching state of the next control cycle. Whereas, variable switching frequency is introduced, which causes difficulty in cooling system and filter design [39]. Furthermore, high performance is at the expense of high computation burden, due to the fact that the number of switching states increase exponentially with the increase of power devices' number, such as the qZS-MCC with numbers of SMs in cascade, while all the states have to be evaluated within one control cycle [42]. A discrete-time average model-based predictive control was proposed for the three-phase qZSI by predicting the ST duty cycle and modulation waves [43], and a dead-beat control was developed to estimate the modulating waves of a three-phase rectifier [44], whereas, only constant dc/ac voltage source and standalone loads are discussed. The qZS-MCC PV power system has to consider also the system-level control functions, such as PV MPPT, dc grid integration, dc-link voltage balance, and cascaded voltage output.

This article proposes a duty-cycle predictive control for the qZS-MCC PV power system, featuring a comprehensive controller design with simple implementation while maintaining fast and accurate tracking capability. The ST duty cycles for dc-link voltage balance and total active-state duty cycle for dc grid power injection are predicted through the derived discrete-time models and feedbacks in real time, while a PI regulator of each SM tracks MPPT of PV panels. In the proposed control, no parameter design efforts are needed in the predictive loop, thus, the controller design is much simplified when compared to PI-based control. The predicted control variables are provided to the qZS-MCC modulator, thus switching control signals with constant switching frequency are fulfilled. The prediction process is executed once in each control cycle based on the derived predictive models, rather than evaluating a cost function for all available switching states, so the computation burden is significantly reduced when compared with the conventional MPC method. That benefit is especially critical for a number of SMs cascaded qZS-MCC.

The paper is structured as follows: Section II introduces the qZS-MCC PV power system; Section III details the proposed predictive control of the system, including grid-connected current, MPPT, and dc-link voltage control; Section IV illustrates simulation and experimental results, and comparison results with the PI-based control of qZS-MCC, followed by the conclusion in Section IV.

II. QZS-MCC PV POWER SYSTEM

Fig. 1 shows the topology of qZS-MCC for dc collection of PV power. HB formed SMs are cascaded to increase output voltage. An isolated HB converter is inserted into the front end of each SM to isolate the PV panel from the high voltage grid. Hence, the qZS-MCC can achieve a voltage much higher than PV panel's insulation voltage. Several qZS-MCC PV systems can be simply integrated at the high-voltage dc bus [9], [11].

A qZS network, consisted of two inductors, two capacitors, and one diode, is embedded into the post stage of HB SM. In one control period T_s, each qZS-HB SM possesses the ST state and non-ST state. The latter includes active state and traditional zero state. Fig. 2 shows the equivalent circuit of post-stage qZS-HB SM, illustrated by SM_1. As shown in Fig. 2 (a), when the ST occurs, both post-stage switches S_{b11} and S_{b12} turn on, the dc-link voltage v_{DC1} is zero. From Fig. 2 (b), during the active state of non-ST state, the upper switch S_{b11} is on while the lower one S_{b12} is off; the output voltage v_{o1} is high with the amplitude of dc-link peak voltage V_{DC}. In the

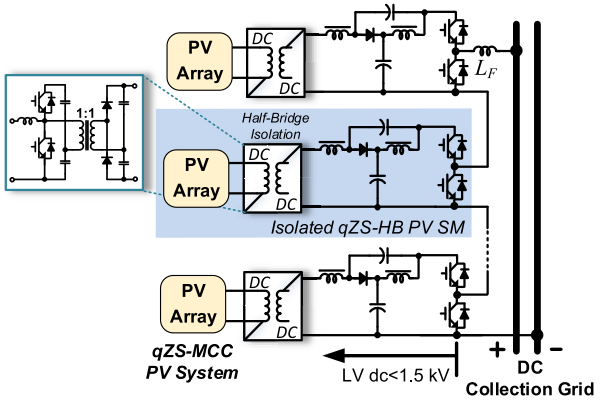

FIGURE 1. The qZS-MCC PV power system integrated into dc grid.

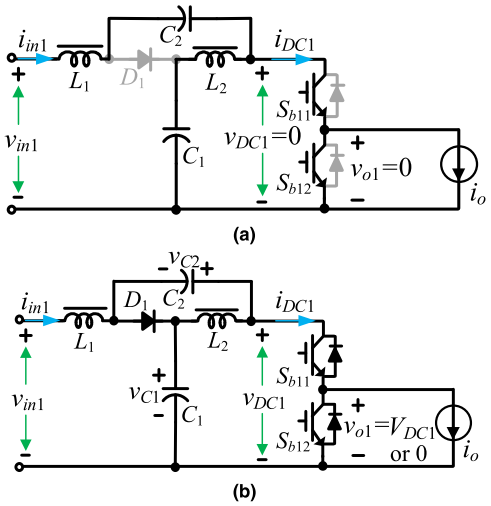

FIGURE 2. The qZS-HB SM_1 in the (a) ST state and (b) non-ST state.

zero state of non-ST state, the anti-parallel diode of S_{b12} freewheels and the output voltage v_{o1} becomes zero.

The qZS-HB does not contribute to the output voltage in the zero and ST states. Then the qZS-MCC's output voltage is summarized as

$$v_o = \sum_{k=1}^{n} v_{ok} = \sum_{k=1}^{n} S_k V_{DCk} \tag{1}$$

And its average dc value is

$$V_o = \sum_{k=1}^{n} V_{ok} = \sum_{k=1}^{n} M_k V_{DCk} \tag{2}$$

where $S_k \in \{0, 1\}$ denotes the switching function of the kth SM's post-stage HB, V_{DCk} denotes the dc-link peak voltage of the kth SM, V_{ok} denotes the average dc output voltage of the kth SM, and M_k denotes the active-state duty cycle of the kth SM, $k \in \{1, \ldots, n\}$ denotes the SM number.

The kth SM's dc-link peak voltage, and voltages of capacitors C_1 and C_2 are, respectively [25]

$$V_{DCk} = \frac{1}{1-2D_k} v_{ink}, \quad V_{C1k} = \frac{1-D_k}{1-2D_k} v_{ink}, \; V_{C2k} = \frac{D_k}{1-2D_k} v_{ink} \tag{3}$$

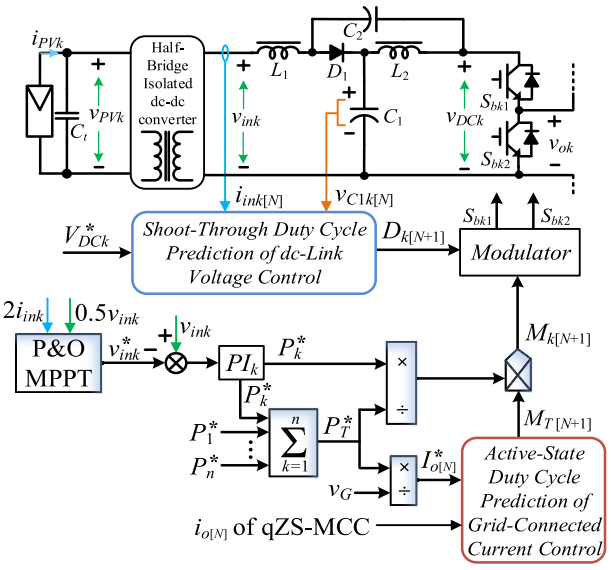

FIGURE 3. Proposed duty-cycle predictive control of the qZS-MCC PV power system.

where D_k denotes the ST duty cycle of the kth SM, and v_{ink} denotes the qZS-network input voltage from the HB isolated converter of the kth SM.

Inherited from qZS converters and through regulating the ST duty cycle in (3), the post-stage qZS-HB is able to handle variations of the input voltage v_{ink}. A high-frequency transformer with 1:1 turn ratio is combined with the front-end HB switches, S_{fk1} and S_{fk2}, to achieve voltage isolation. When a constant duty cycle $D_0 = 0.5$ is used, the output voltage is doubled [11]. Namely, there are

$$\begin{aligned} v_{ink} &= v_{PVk}/D_0 = 2v_{PVk}, \\ i_{ink} &= D_0 i_{PVk} = i_{PVk}/2 \end{aligned} \tag{4}$$

This design can achieve benefits as follows: i) isolation between PV panel and high voltage grid; ii) PV voltage boost; iii) the maximum utilization of the HB isolated converter [11]; iv) low size of transformer; v) simple control implementation due to constant duty cycle of 0.5.

III. PROPOSED DUTY-CYCLE PREDICTIVE CONTROL OF QZS-MCC PV POWER SYSTEM

Fig. 3 shows the block diagram of proposed control method for the qZS-MCC based high-voltage PV power system. The control targets include MPPT of isolated PV arrays, SMs' dc-link voltage balance, and power injection into dc collection grid. As Fig. 3 shows, the ST duty cycle $D_{k[N+1]}$ of each SM and global active-state duty cycle $M_{T[N+1]}$ in the next control cycle are predicted to achieve dc-link voltage control and grid-connected current control, respectively. Therewith, the $M_{T[N+1]}$ is utilized to obtain the active-state duty cycle $M_{k[N+1]}$ of each SM according to PI-based MPPT. The predictions $D_{k[N+1]}$ and $M_{k[N+1]}$ are then applied to the qZS-MCC's modulator in the next sampling instant. Hence, the n+1 predictive loops and n PI regulators fulfill the control targets.

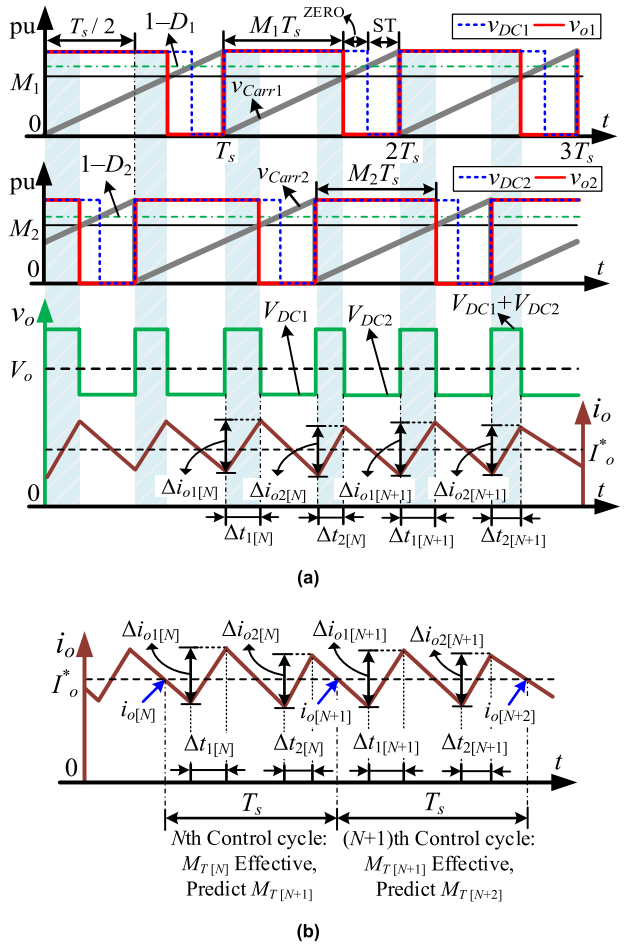

FIGURE 4. Sketch map of qZS-MCC output voltage and grid-connected current by two modules. (a) Typical waveforms, and (b) illustration of the prediction algorithm.

A. MPPT AND GRID-CONNECTED CURRENT CONTROL

1) PREDICTION OF GLOBAL ACTIVE-STATE DUTY CYCLE

Fig. 4 shows the sketch map of qZS-MCC output voltage and grid-connected current with the modulation of qZS-MCC, using two SMs as an example, where Fig. 4 (a) shows the typical waveforms and Fig. 4 (b) illustrates the prediction algorithm. From Fig. 4 (a), it can be seen that each SM has the time duration of M_kT_s in active state, and $(1-M_k)T_s$ in zero and ST states during one control cycle T_s, $k\in\{1, 2\}$. When both SMs are in the active state, the qZS-MCC output voltage v_o is the sum of two SMs' dc-link peak voltage $V_{DC1}+V_{DC2}$, and the filter inductor is charged leading to an increasing of the grid-connected current i_o. Otherwise, the v_o will be one SM's dc-link peak voltage V_{DC1} or V_{DC2}, and the filter inductor gets discharged, causing i_o to decrease. The dc-link voltages are balanced and keep constant under the well-developed control. Hence, when all SMs are in the active state, there is dynamic of

$$L_F\frac{di_o(t)}{dt}=nV_{DC}-v_G-R_Ei_o(t) \tag{5}$$

where $V_{DC}=V_{DC1}=V_{DC2}=\ldots=V_{DCn}$ denotes the constant dc-link peak voltage of all SMs, v_G denotes the dc grid voltage, L_F denotes filter inductance, and R_E denotes internal resistance.

When any SM is in zero or ST states, there is

$$L_F\frac{di_o(t)}{dt}=(n-1)V_{DC}-v_G-R_Ei_o(t) \tag{6}$$

As shown in Fig. 4 (a), there is a 180° phase difference between carriers v_{Carr1} and v_{Carr2} of the two SMs. Use v_{Carr1} as reference. In one control cycle, the current increments are $\Delta i_{o1[N]}$ and $\Delta i_{o2[N]}$, respectively, in $\Delta t_{1[N]}$ and $\Delta t_{2[N]}$ durations, due to the charging action of filter inductor when both SMs are in the active-state duty cycle. Therefore, the total current increment $\Delta i_{o[N]}=\Delta i_{o1[N]}+\Delta i_{o2[N]}$ in the Nth control cycle is related to the time duration of $\Delta t_{1[N]}+\Delta t_{2[N]}=[M_1-(1-M_2)]T_s$. Correspondingly, the current decreases for the duration $T_s-(\Delta t_{1[N]}+\Delta t_{2[N]})=T_s-[M_1-(1-M_2)]T_s=[2-(M_1+M_2)]T_s$ when any SM is in zero or ST states.

Similarly, for n SMs, the sum of active-state duty cycles in the Nth control cycle is noted as $M_{T[N]}=M_1+M_2+\ldots+M_n$. With (5) and (6), the derivation of grid-connected current with respect to the current increment and decrement durations are expressed as, respectively,

$$\frac{di_{o[N]}}{dt}=\begin{cases}\dfrac{nV_{DC}-v_G-R_Ei_{o[N]}}{L_F} & \text{in } \left[M_{T[N]}-(n-1)\right]T_s\\ \dfrac{(n-1)V_{DC}-v_G-R_Ei_{o[N]}}{L_F} & \text{in } \left(n-M_{T[N]}\right)T_s\end{cases} \tag{7}$$

Using Euler method, the discrete current derivation holds

$$\frac{di_{o[N]}}{dt}=\frac{\Delta i_{o[N]}}{\Delta T}=\frac{i_{o[N+1]}-i_{o[N]}}{T_s} \tag{8}$$

From (7) and (8), the average grid-connected current in one control cycle will be

$$\begin{aligned}&\frac{i_{o[N+1]}-i_{o[N]}}{T_s}\\&=\frac{nV_{DC}-v_G-R_Ei_{o[N]}}{L_F}\left[M_{T[N]}-(n-1)\right]\\&\quad+\frac{(n-1)V_{DC}-v_G-R_Ei_{o[N]}}{L_F}\left(n-M_{T[N]}\right)\end{aligned} \tag{9}$$

Hence, through (9), it can be derived that

$$i_{o[N+1]}=\frac{T_s}{L_F}\left(M_{T[N]}V_{DC}-v_G\right)+\left(1-\frac{T_sR_E}{L_F}\right)i_{o[N]} \tag{10}$$

From (10) and Fig. 4 (b), at the end of the Nth control cycle, i.e., the beginning of the $(N+1)$th control cycle, the grid-connected current is controlled to $i_{o[N+1]}$ through $M_{T[N]}$. Therewith, at the end of the $(N+1)$th control cycle, the current $i_{o[N+2]}$ can be obtained as

$$i_{o[N+2]}=\frac{T_s}{L_F}\left(M_{T[N+1]}V_{DC}-v_G\right)+\left(1-\frac{T_sR_E}{L_F}\right)i_{o[N+1]} \tag{11}$$

from the effort of $M_{T[N+1]}$.

The control goal of $M_{T[N]}$ is to ensure $i_{o[N+1]}=I^*_{o[N+1]}$ at the end of the Nth control cycle. The cost function of

grid-connected current control for the Nth control cycle is defined as

$$g_{io[N]} = \left| I^*_{o[N+1]} - i_{o[N+1]} \right| \tag{12}$$

When the control is well worked, the grid-connected current $i_{o[N+1]}$ tracks well with the reference current $I^*_{o[N+1]}$ at the end of the Nth control cycle through $M_{T[N]}$, i.e., $g_{io[N]} = 0$. Similarly, there are $g_{io[N+1]} = 0$ and $i_{o[N+2]} = I^*_{o[N+2]}$ at the end of the $(N+1)$th control cycle through $M_{T[N+1]}$. At the much small sampling time, it is effective that $I^*_{o[N+2]}$=$I^*_{o[N+1]} = I^*_{o[N]}$, i.e.,

$$i_{o[N+2]} = I^*_{o[N]} \tag{13}$$

where $I^*_{o[N]}$ denotes the reference grid-connected current.

Substituting (10) and (13) into (11), the global active-state duty cycle for the $(N+1)$th control cycle can be predicted by

$$M_{T[N+1]} = \frac{L_F}{T_s V_{DC}} \left[I^*_{o[N]} - \left(1 - \frac{T_s R_E}{L_F} \right)^2 i_{o[N]} \right] - \left(1 - \frac{T_s R_E}{L_F} \right) M_{T[N]} + \frac{v_G}{V_{DC}} \left(2 - \frac{T_s R_E}{L_F} \right) \tag{14}$$

2) DUTY CYCLE DISTRIBUTION FOR MPPT

As the proposed control shown in Fig. 3, the error between actual post-stage qZS-HB input voltage v_{ink} and reference voltage v^*_{ink} is compensated by a PI regulator in each SM, acquiring the maximum point power P^*_k of the kth SM. In order to inject the maximum point power of each SM into the dc collection grid, the predicted global active-state duty cycle $M_{T[N+1]}$ for the next control cycle is distributed to the kth SM's active-state duty cycle $M_{k[N+1]}$ by

$$M_{k[N+1]} = \frac{P^*_k}{P^*_T} M_{T[N+1]} \tag{15}$$

where $P^*_T = P^*_1 + P^*_2 + \ldots + P^*_n$ denotes the sum of n SMs' maximum point powers.

Due to the constant 50% duty cycle of the front-end isolation converter, the qZS-HB input voltage v_{ink} and current i_{ink} are measured to perform the perturbation and observation MPPT, obtaining the reference voltage v^*_{ink} of the kth SM.

Furthermore, to interface with the dc collection grid and inject all the collected PV power into the grid, the reference grid-connected current in (12) is determined by

$$I^*_{o[N]} = \frac{P^*_T}{v_G} \tag{16}$$

Hence, the predictive control and distribution of global active-state duty cycle and the PI-based input voltage control achieve the grid-connected current control and PV MPPT.

B. DC-LINK VOLTAGE BALANCE CONTROL

Each SM's post-stage qZS-HB operates independently at its own ST and non-ST states, according to the on-off states of switches S_{bk1} and S_{bk2}. In the ST state, the PV panel and qZS capacitors charge the qZS inductors, therefore, the qZS inductor currents increase while qZS capacitor voltages decreasing. In the non-ST state, the PV panel and qZS inductors charge the qZS capacitors and provide power to the load, with qZS inductor currents decreasing and qZS capacitor voltages increasing.

Under $L_1 = L_2 = L$ and $C_1 = C_2 = C$, dynamic equation of the kth SM's qZS network is simplified as a second-order system [45], [46]. In the ST state, there are

$$L \frac{di_{ink}(t)}{dt} = v_{C1k}(t) - (R + r) i_{ink}(t) \tag{17}$$

$$C \frac{dv_{C1k}(t)}{dt} = -i_{ink}(t) \tag{18}$$

where r and R denote the internal resistance of qZS inductor and capacitor, respectively.

The non-ST state yields

$$L \frac{di_{ink}(t)}{dt} = v_{ink} - v_{C1k}(t) - (R + r) i_{ink}(t) + R i_{DCk} \tag{19}$$

$$C \frac{dv_{C1k}(t)}{dt} = i_{ink}(t) - i_{DCk} \tag{20}$$

where i_{DCk} denotes the dc-link current of the kth qZS-HB SM.

Similarly, for the ST state in time duration $D_{k[N]}T_s$ and the non-ST state in time duration $(1-D_{k[N]})T_s$, the average qZS inductor current and capacitor voltage in one control cycle are, respectively

$$\frac{i_{ink[N+1]} - i_{ink[N]}}{T_s} = \frac{v_{C1k[N]} - (R + r) i_{ink[N]}}{L} D_{k[N]} + \frac{v_{ink} - v_{C1k[N]} - (R + r) i_{ink[N]} + R i_{DCk}}{L} \left(1 - D_{k[N]} \right) \tag{21}$$

$$\frac{v_{C1k[N+1]} - v_{C1k[N]}}{T_s} = \frac{-i_{ink[N]}}{C} D_{k[N]} + \frac{i_{ink[N]} - i_{DCk}}{C} \left(1 - D_{k[N]} \right) \tag{22}$$

where $D_{k[N]}$ denotes the kth SM's ST duty cycle in the Nth control cycle.

From (21) and (22), the qZS inductor current $i_{ink[N+1]}$ and capacitor voltage $v_{C1k[N+1]}$ at the end of Nth control cycle can be derived. Therewith, the qZS-HB input current i_{ink} and capacitor-C_1 voltage v_{C1k} at the end of $(N+1)$th control cycle can be obtained by

$$i_{ink[N+2]} = \frac{T_s}{L} \left[\left(2D_{k[N+1]} - 1 \right) v_{C1k[N]} + \left(1 - D_{k[N+1]} \right) v_{ink} + \left(1 - D_{k[N+1]} \right) R i_{DCk} \right] + \left[1 - \frac{T_s (R + r)}{L} \right] i_{ink[N+1]} \tag{23}$$

$$v_{C1k[N+2]} = \frac{T_s}{C} \left[\left(1 - 2D_{k[N+1]} \right) i_{ink[N+1]} - \left(1 - D_{k[N+1]} \right) i_{DCk} \right] + v_{C1k[N+1]} \tag{24}$$

The control objective of ST duty cycle $D_{k[N]}$ is to ensure a zero tracking error between the reference dc-link peak voltage $V^*_{DCk[N+1]}$ and the actual peak voltage $V_{DCk[N+1]}$, besides a zero error between the reference qZS-HB input current $I^*_{ink[N+1]}$ and actual current $i_{ink[N+1]}$, at the end of Nth control cycle. Then, the cost function of dc-link voltage control for the kth SM is defined as

$$g_{k[N]} = \left|V^*_{DCk[N+1]} - V_{DCk[N+1]}\right| + \left|I^*_{ink[N+1]} - i_{ink[N+1]}\right| \tag{25}$$

Similar to the derivation of grid-connected current control, there is $g_{k[N+1]} = 0$ through the effort of $D_{k[N+1]}$ at the end of the $(N+1)$th control cycle, when the control is well operated. Taking into account much small sampling time and from (3), there are

$$V_{DCk[N+2]} = \frac{v_{C1k[N+2]}}{1 - D_{k[N+1]}} = V^*_{DCk[N]} \tag{26}$$

$$i_{ink[N+2]} = I^*_{ink[N]} \tag{27}$$

Substituting (26) into (24) and (27) into (23), respectively, the reference qZS-HB input current $I^*_{ink[N]}$ can be obtained by

$$I^*_{ink[N]} = \frac{CV^*_{DCk}\left(1 - D_{k[N]}\right) - Cv_{C1k[N]}}{T_s\left(1 - 2D_{k[N]}\right)} + \frac{2\left(1 - D_{k[N]}\right)}{1 - 2D_{k[N]}} i_{DCk} - i_{ink[N]} \tag{28}$$

And with the $i_{ink[N+1]}$ and $v_{C1k[N+1]}$ from (21) and (22), the $D_{k[N+1]}$ for the next control cycle is predicted by

$$D_{k[N+1]} = \frac{LI^*_{ink[N]} \Big/ T_s - a_1^2 i_{ink[N+1]} - a_1\left(a_2 D_{k[N]} + a_3\right) - a_3}{a_2} \tag{29}$$

where $a_1 = 1 - T_s(R + r)/L$, $a_2 = 2v_{C1k[N]} - v_{ink} - Ri_{DCk}$, $a_3 = v_{ink} + Ri_{DCk} - v_{C1k[N]}$.

Then, at the identical dc-link voltage references $V^*_{DC1[N+1]} = V^*_{DC2[N+1]} = \ldots = V^*_{DCn[N+1]} = V^*_{DC[N+1]}$, all the n SMs' dc-link peak voltages will be balanced for the $(N+1)$th control cycle, even though the PV panel voltage varies.

C. IMPLEMENTATION AND ADVANTAGES

According to Fig. 3, the steps to implement the proposed duty-cycle predictive control of qZS-MCC system are shown as follows.

i) At the beginning of the Nth control cycle, the grid-connected current $i_{o[N]}$ is measured to predict the global active-state duty cycle $M_{T[N+1]}$ through (14), for the $(N+1)$th control cycle.

ii) With the PI-based MPPT control, the active-state duty cycle $M_{k[N+1]}$ of the kth SM is obtained through (15).

iii) The kth SM's qZS-HB input current $i_{ink[N]}$ and qZS capacitor-C_1 voltage $v_{C1k[N]}$ are measured to predict the ST duty cycle $D_{k[N+1]}$ of the kth SM by (29), for the $(N+1)$th control cycle.

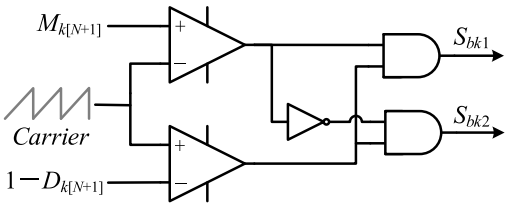

FIGURE 5. Schematic of the qZS-HB modulator.

iv) The predicted $M_{k[N+1]}$ and $D_{k[N+1]}$ are then applied to the modulator of qZS-MCC in the beginning of the $(N+1)$th control cycle to achieve the control goals.

Fig. 5 shows the schematic of qZS-HB modulator to combine the $M_{k[N+1]}$ and $D_{k[N+1]}$. A saw tooth carrier at the switching frequency is compared with the $M_{k[N+1]}$ and $1 - D_{k[N+1]}$ of the kth SM. When the carrier is higher than $1 - D_{k[N+1]}$, a ST state is produced by turning on the two switches S_{bk1} and S_{bk2} of the post-stage phase leg simultaneously. Otherwise, the S_{bk1} and S_{bk2} work oppositely depending on the relationship between the $M_{k[N+1]}$ and carrier. If $M_{k[N+1]}$ is higher than the carrier, S_{bk1} is ON, otherwise, it is OFF, and S_{bk2} is completely opposite to S_{bk1}.

It can be seen that the proposed control applies one PI regulator and one predictive loop of each SM, as well as one predictive loop of the system current control, i.e., n PI regulators and $n+1$ predictive loops of the control system. Table 1 shows the controller design, computation, and parameters of the proposed, PI-based, and conventional MPC methods. Comparing to the latter two, the advantages of proposed control are listed as follows.

i) The cost function is defined to zero, as a result that there is no cost function calculation required in the proposed control method. It overcomes the disadvantage of the conventional MPC that needs to calculate a cost function in each control cycle. According to the conventional MPC, the more the cascaded SMs, the heavier the computation burden, which grows exponentially with the switching devices. Therefore, the computation effort is much reduced for the qZS-MCC using the proposed control.

It should be highlighted that the cost function of conventional MPC causes the two main issues: first, it is hard to choose best weighting factors for the cost function because there is no theory to support its design, and trial and error method is the only way; second, sometimes the chosen weighting factors may cause a stability issue at some operation conditions and its reliability and robustness are concerns. These disadvantages are the main challenges for the conventional MPC in application to the qZS-MCC because immense weighting factors are needed. The proposed control fully overcomes these issues.

ii) The proposed control predicts the duty cycles of the next control cycle to achieve the control goals through the modulator, as shown in Fig. 5. As a result, a constant switching frequency is achieved. This avoids disadvantage of the conventional MPC that has a variable switching frequency. It can be seen that the switching frequency of the proposed control method is controlled as needed.

TABLE 1. Comparison of Proposed, PI-Based, and Conventional MPC Methods.

Items	*Proposed Control*	*PI-Based Control*	*Conventional MPC*
Number of regulators	n PI regulators plus (n+1) predictive regulators	(2n+1) PI regulators and n P regulators	n PI regulators plus (n+1) predictive regulators
Cost function No.	None	None	n+1
Control computation burden	Low	Medium	High
Execution time*	49.9 μs	53.8 μs	N/A
Memory requirement*	23.6 KB	29.2 KB	N/A
Modulator No.	n	n	None
Switching frequency	Constant	Constant	Variable
Parameters design	Parameters of n PI regulators are designed.	Parameters of (2n+1) PI regulators and n P regulators are designed.	Parameters of n PI regulators and weighting factors of (n+1) cost functions.

*Note: The data are provided for two SMs formed qZS-MCC PV system.

A high switching frequency will reduce the size of passive components, such as QZS inductors and capacitors and filter inductor, but switching power loss will be increased. A small switching frequency will lower the switching power loss, but increase passive components size.

iii) The controller design and implementation are much simple because there are no controller parameters required in the predictive control loops. For instance, no weighting factors as the conventional MPC or proportional and integral parameters as the PI-based control are involved.

Each SM has one PI regulator only for achieving MPPT in the proposed control. This PI regulator can be designed by employing typical Bode plot design method [14]. In addition, the SMs' PI and predictive control are independently implemented. Therefore, a modular and scalable design will be easily realized for the qZS-MCC when numbers of SMs are cascaded to achieve a high voltage.

IV. SIMULATION AND EXPERIMENTAL INVESTIGATIONS

A qZS-MCC PV system consisted of two front-end isolated qZS-HB SMs is built. The proposed duty-cycle predictive control is implemented and compared with the conventional PI-based control of the qZS-MCC PV system.

To make the comparison of the two methods under the same condition, the qZS inductance and capacitance values and PI regulator's parameters of MPPT control in simulation and experiment are selected according to those in [10] and [12], where the qZS inductance is designed to limit the peak-to-peak switching frequency ripple of qZS inductor current within 20% and the qZS capacitance is to buffer the peak-to-peak switching frequency ripple of dc-link peak voltage within 1%. Table 2 lists the simulation and prototype parameters. Table 3 lists the controller parameters of the PI-based control.

Fig. 6 (a) shows a high-level schematic of the experimental system, and Fig. 6 (b) shows the experimental setup. Each SM's qZS-network inductors are built on the coupled AMCC-250 core. The TMS320F28335 based digital signal processor (DSP) control board performs the proposed control method. As shown in Fig. 6, the front-end HB of SM_1 and SM_2 share one PWM register that the same signal

TABLE 2. System specifications.

Simulation System Parameters	*Values*
Rated power of one SM, P_m	60 kW
qZS-HB input voltage range, v_{ink}	350~600 V
Averagedc output voltage of one SM, V_{ok}	600 V
Total dc output voltage, V_{dc}	1200 V
Switching frequency	10 kHz
qZS inductance, L_1 and L_2	750 μH coupling
qZS capacitance, C_1 and C_2	1100 μF
Prototype Parameters	***Values***
Rated power of one SM, P_m	1 kW
qZS-HB input voltage range, v_{ink}	55~100 V
Average dc output voltage of one SM, V_{ok}	100 V
Total dc output voltage, V_{dc}	200 V
Switching frequency	10 kHz
qZS inductance, L_1 and L_2	550 μH coupling
qZS capacitance, C_1 and C_2	680 μF

TABLE 3. Controller parameters of PI-based control.

Parameters	*Values*
Proportional parameter of grid-connected current control	0.0047
Integral parameter of grid-connected current control	3.11
Proportional parameter of MPPT control	274.5
Integral parameter of MPPT control	0.5
Proportional parameter of dc-link voltage control outer loop	0.1
Integral parameter of dc-link voltage control outer loop	40
Proportional parameter of dc-link voltage control inner loop	0.002

is sent to the upper switches S_{f11} and S_{f21}, and the lower switches S_{f12} and S_{f22}. The two SMs' qZS-HB input currents $i_{in\ 1[N]}$ and $i_{in\ 2[N]}$, input voltages $v_{in\ 1[N]}$ and $v_{in\ 2[N]}$, qZS-network capacitor-C_1 voltages $v_{C11[N]}$ and $v_{C12[N]}$, and grid-connected current $i_{o[N]}$ are measured and sent to the analog to digital converter (ADC) of the DSP in the present control cycle. After performing the control and modulation algorithms, the switching control signals are obtained for the post-stage qZS-HB of the two SMs through one pulse width modulation (PWM) register for each SM. The signals are sent to the SM_1 switches S_{b11} and S_{b12}, and SM_2 switches S_{b21} and S_{b22}, respectively, at the beginning of next control cycle.

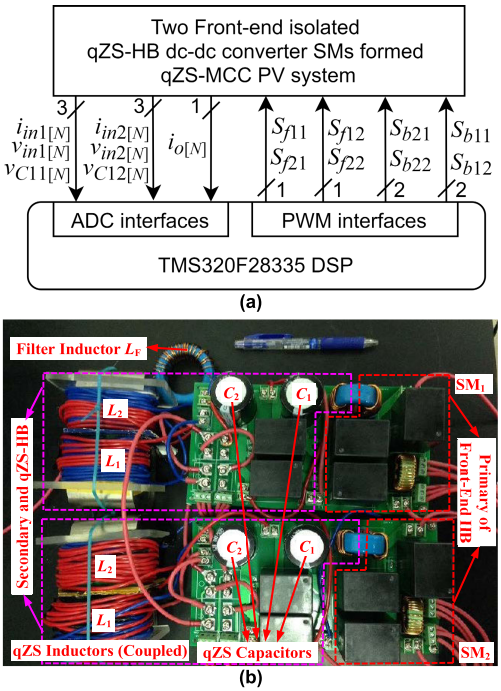

FIGURE 6. Experimental system. (a) Schematic, (b) setup.

In the investigations, simulation and experimental tests are firstly carried out for the proposed duty-cycle predictive control of the qZS-MCC PV system. The two SMs operate at the same condition at the beginning. A sudden irradiance increase from 600 W/m^2 to 1000 W/m^2 is applied to the SM_1's PV panel at 0.5 s in simulation. In the experimental tests, the PV panels of two SMs are working at 25 $^\circ$C and 600 W/m^2 at the beginning; then the irradiance of SM_1 increases to 1000 W/m^2 by regulating solar array simulator. Results shown in Figs. 7 and 8, respectively. For the comparison, the PI-based control of qZS-MCC in [10], [12] is tested on the built prototype. Similar condition of sudden irradiance increase is performed to SM_1 from 600 W/m^2 to 1000 W/m^2, as results shown in Fig. 9.

A. SIMULATION AND EXPERIMENTAL RESULTS

1) RESULTS OF PROPOSED PREDICTIVE CONTROL

Figs. 7 and 8 show simulation and experimental results of qZS-MCC using the proposed control. From the two SMs' PV panel currents i_{PV1} and i_{PV2} and voltages v_{PV1} and v_{PV2} of Figs. 7 (a) and 8 (a), it can be seen that the rise of SM_1's irradiance results in increase of the PV panel current and voltage in SM_1. Furthermore, due to the constant 50% duty cycle of the front-end isolation converter, the input voltage $v_{in\ 1}$ and current $i_{in\ 1}$ of SM_1's post-stage qZS-HB match (4) and increase as well, as Figs. 7 (a) and 8 (b) shown. Whereas, those of SM_2 remain unchanged.

From Fig. 7 (c), the SM_1's ST duty cycle D_1 decreases and that of SM_2 has no change when the qZS-HB input voltage of SM_1 increases. The D_1 and D_2 are controlled to maintain constant dc-link peak voltage. As a result, it can be seen in Figs. 7 (b) and 8 (c), the peak value of SM_1's dc-link voltage

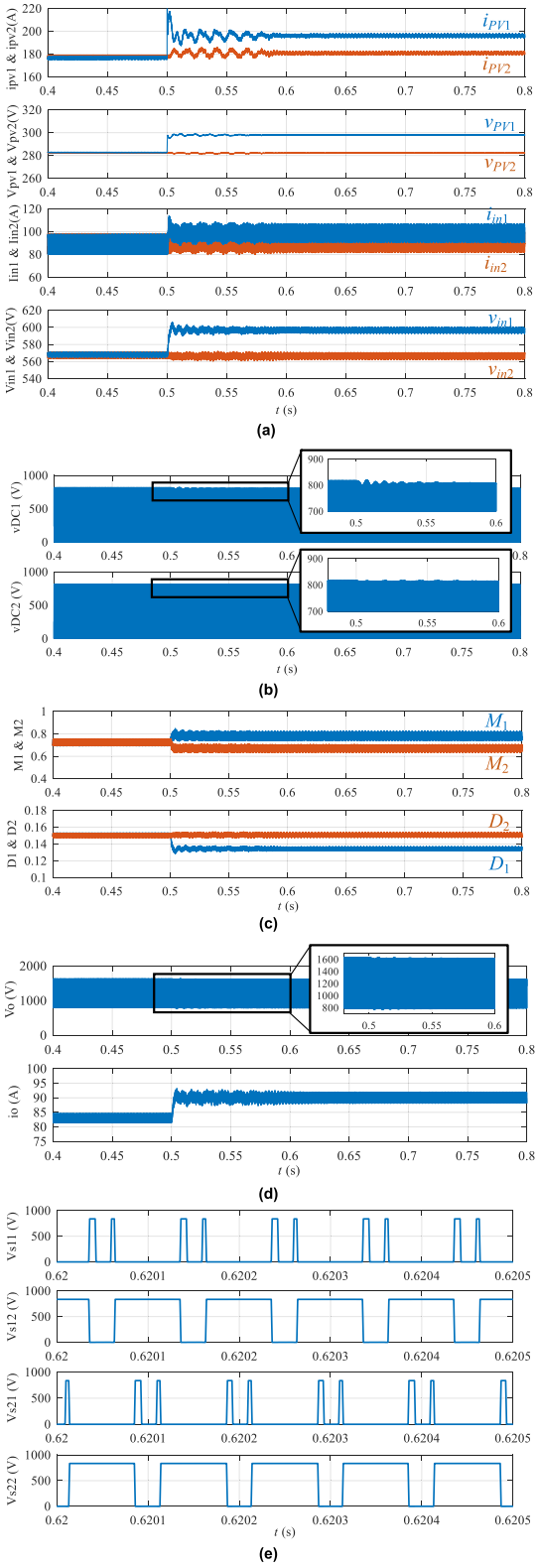

FIGURE 7. Simulation results of SM_1 and SM_2's (a) PV panel currents i_{PV1} and i_{PV2}, PV panel voltages v_{PV1} and v_{PV2}, qZS-HB input currents i_{in1} and i_{in2}, and qZS-HB input voltages v_{in1} and v_{in2}; (b) dc-link voltages v_{DC1} and v_{DC2}; (c) active-state duty cycles M_1 and M_2, and ST duty cycles D_1 and D_2; (d) qZS-MCC's output voltage v_o and grid-connected current i_o; as well as (e) voltages of SM_1 and SM_2's qZS-HB switches at the proposed predictive control.

v_{DC1} recovers to the starting value after a short adjusting time, while that of SM_2 remaining unchanged. In consequence, the peak value of qZS-MCC output voltage v_o maintains the same, as Figs. 7 (d) and 8 (d) show, regardless of the PV panel voltage variation in SM_1.

Also, from Fig. 7 (c), it can be seen that the active-state duty cycle M_1 of SM_1 increases and that of SM_2 decreases, which handles the power difference between the two SMs. In addition, from the increased grid-connected current i_o and unchanged qZS-MCC output voltage v_o of Figs. 7 (d) and 8 (d), it can be obtained that the increased PV power of SM_1 caused by irradiance rising is injected into dc collection grid.

It is noted that the proposed predictive control achieves fast and accurate tracking for the qZS-MCC, with simple control structure and controller design. The circuit voltages and currents of qZS-MCC become stable with a fast response speed after the irradiance change, while a constant switching frequency is achieved, as the voltages of the two SMs' power devices shown in Fig. 7 (e).

2) RESULTS OF PI-BASED CONTROL METHOD

For PI-based control, in each SM, there is one PI regulator based MPPT control adjusting the PV panel voltage, and one dual-loop control, consisted of a PI regulator and a proportional regulator, balancing the dc-link peak voltages. Besides, one PI regulator controls global grid-connected current. Controller parameters are as shown in Table 4. Fig. 9 shows results of two SMs' PV panel currents and voltages, two SMs' qZS-HB input currents and voltages, two SMs' dc-link voltages, as well as grid-connected current and qZS-MCC output voltage, corresponding to those of predictive control in Fig. 8.

From experimental results of Figs. 8 and 9, it can be seen that both methods demonstrate good steady-state stability that the MPPT is well achieved, the dc-link peak voltages are balanced, and the increased PV power is injected into the dc collection grid, even though there are PV panel current and voltage variations. Whereas, the qZS-MCC system shows smaller overshoots and much faster response speed from the proposed predictive control than the PI-based control. From Figs. 8(c) and (d) and 9(c) and (d), the grid-connected current and two SMs' dc-link peak voltage have smaller overshoots under the proposed control than using the PI-based control. It can be seen that the overshoot of SM_1's dc-link voltage v_{DC1} and qZS-MCC output voltage v_o are ignorable, and the currents and voltages become stable within 50 ms, when applying the proposed predictive control. However, a 7.8-V overshoot appears on v_{DC1}, and nearly 500 ms settling time appears to circuit currents and voltages when using the PI-based control.

B. DISCUSSION

From the control block diagram of the proposed duty-cycle predictive control in Fig. 3 and the control block diagram of PI-based control shown in [12], it can be seen that both methods have $2n+1$ control loops. The PI-based control needs to elaborately design $4n+2$ proportional and integral parameters and n proportional parameters through specific small-signal modeling and transfer function derivation.

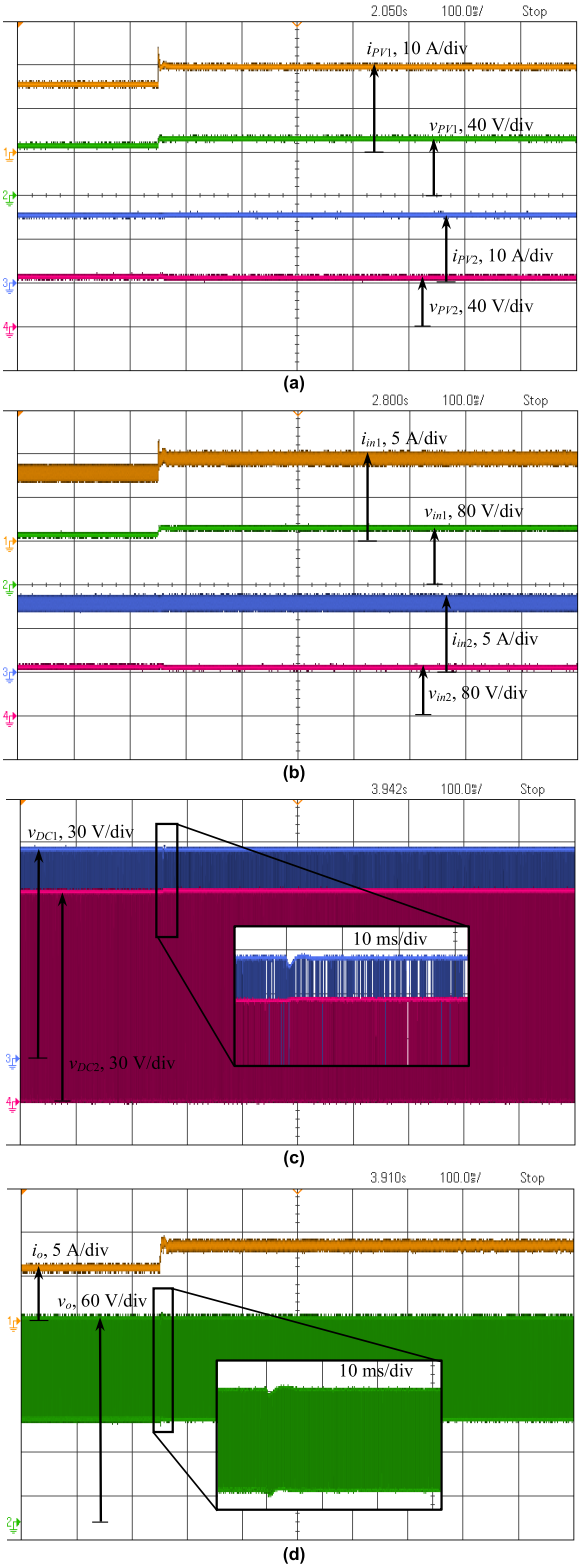

FIGURE 8. Experimental results of (a) two SMs' PV panel currents and voltages, (b) two SMs' qZS-HB input currents and voltages, (c) two SMs' dc-link voltages, and (d) grid-connected current and qZS-MCC output voltage at the proposed predictive control of qZS-MCC PV system.

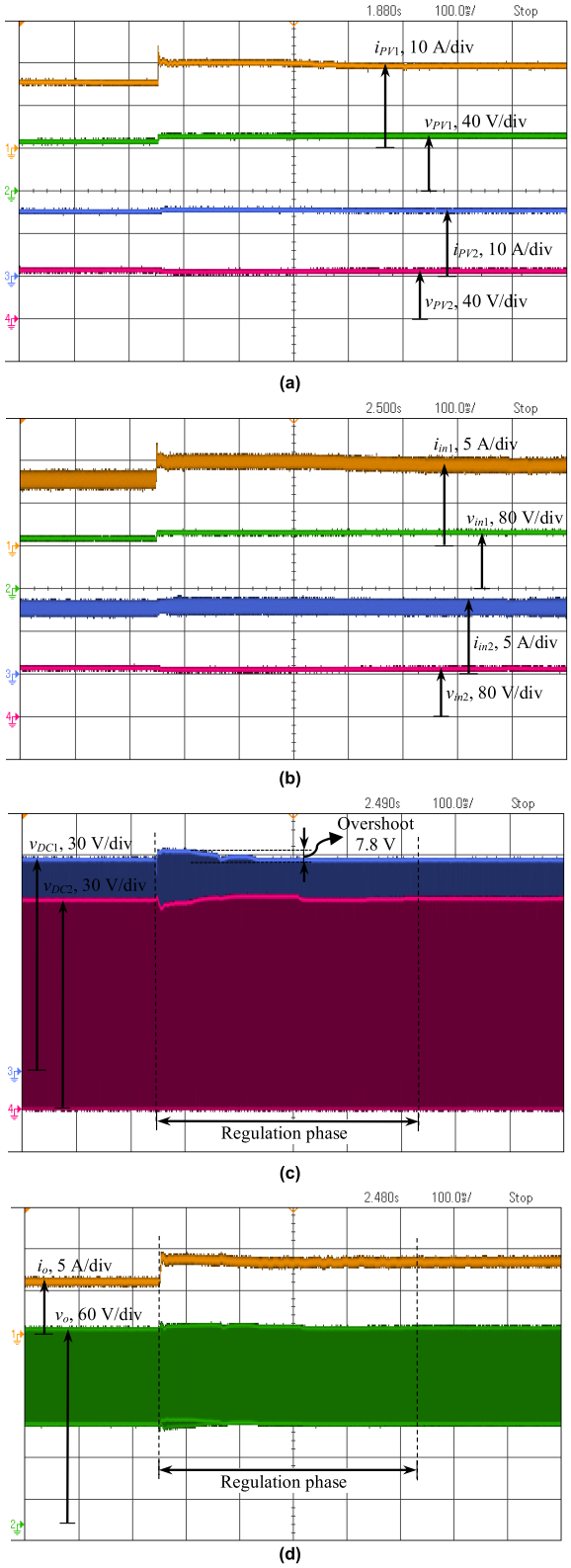

FIGURE 9. Experimental results of (a) two SMs' PV panel currents and voltages, (b) two SMs' qZS-HB input currents and voltages, (c) two SMs' dc-link voltages, and (d) grid-connected current and qZS-MCC output voltage at the PI-based control of qZS-MCC PV system.

Whereas, more than half PI regulators design related efforts are eliminated in the proposed predictive control. The n+1 predictive loops of the proposed control obtain the control

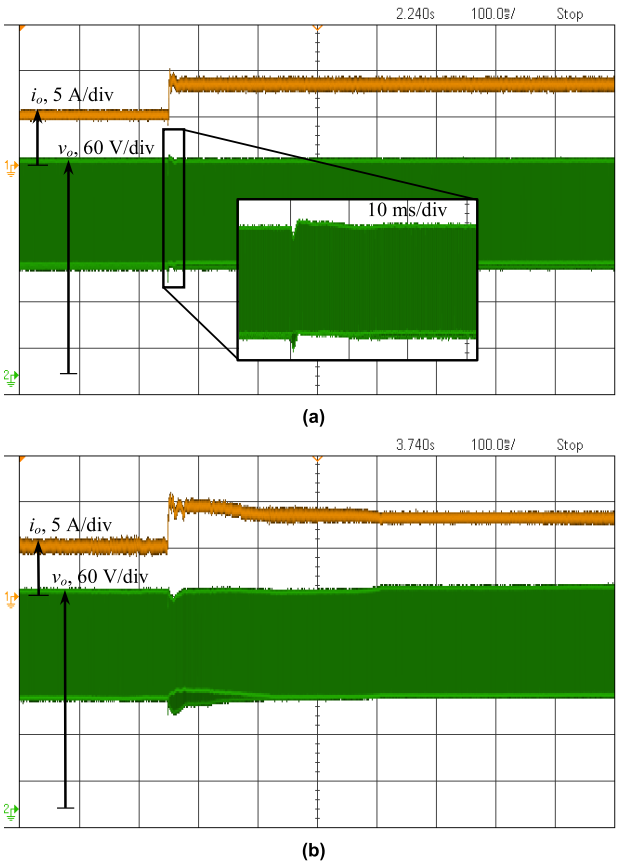

FIGURE 10. Experimental results of grid-connected current and qZS-MCC output voltage when SM_1's irradiance changes from 400 W/m^2 to 1000 W/m^2. (a) Proposed predictive control, and (b) PI-based control.

variables of ST duty cycles and active-state duty cycles through the derived discrete-time circuit model, without need of tough PI parameters design.

From Figs. 7-9, it can be seen that both methods achieve accurate steady-state stability of circuit voltages and currents. Whereas, the dynamic responses of qZS-MCC system are much faster when using the proposed control than with PI-based control. In addition, the proposed control method shows high robustness, even though the duty-cycle predictive model involves circuit parameters.

Moreover, less design parameters in the proposed control method also simplifies the design, which enhances the system reliability. The grid-connected current and qZS-MCC output voltage are tested when a wide irradiance change from 400 W/m^2 to 1000 W/m^2 is applied to SM_1. In the tests, all the other controller parameters of the two methods are kept same as the tested condition in Figs. 8 and 9.

Fig. 10 (a) and (b) shows results from the proposed predictive control and PI-based control, respectively. It can be seen that the proposed predictive control still shows smaller overshoots and much faster response speeds than that of the PI-based control in this case. Furthermore, comparing Figs. 8 (d) with 10 (a), and 9 (d) with 10 (b), it can be seen that the proposed predictive control achieves similar response speed and overshoot to the grid-connected current

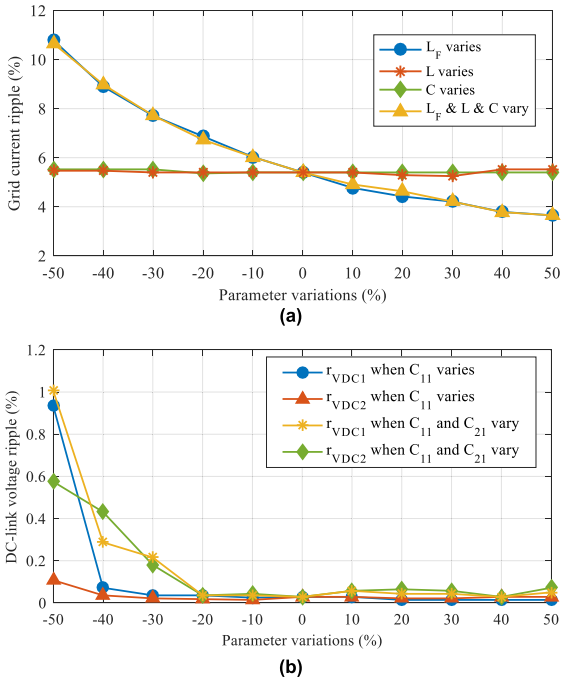

FIGURE 11. Parameter variations. (a) Grid-connected current ripple ratio versus circuit parameters variations, and (b) dc-link peak voltage ripple versus circuit parameters variations.

and qZS-MCC output voltage with the test in Fig. 9. Whereas, larger overshoots and worse response waveforms appear to the current and voltage in Fig. 10 (b) than those in Fig. 9 (d), indicating potential instability of PI regulators when a wider irradiance change occurs.

In summary, the proposed duty-cycle predictive control simplifies the control design and implementation, while improving the performance of the qZS-MCC PV power system in terms of much fast dynamics and high robustness.

C. PARAMETER VARIATIONS

The parameters of passive components, such as qZS-network inductors and capacitors and grid filer inductor, tend to vary, which would result into parameters mismatch between the SMs.

Investigations are carried out on parameters varying of the grid-side filter inductance L_F, qZS-network inductance L, and qZS-network capacitance C in the circuit, while all parameters remaining unchanged in the predictive controller. The $\pm 50\%$ variations from the normal values are conducted on the passive component parameters. Fig. 11 (a) shows the grid-connected current ripple ratio, from the peak-to-peak ripple current to the average current, versus passive component parameters variations. It can be seen that the variations of the grid-side filter inductance has dominant effect than other components. And variations of qZS-network inductance and capacitance have little effects on the grid-connected current ripple. In all cases, the current ripple ratio is almost within 10%, which is absolutely safe from the 20% design criteria, even at the $\pm 50\%$ variations.

The dc-link voltage ripple ratio, from the peak-to-peak ripple voltage to the average value of dc-link voltage, versus different qZS-network capacitance between the two SMs is also investigated. Fig. 11 (b) shows the results, where r_{vDC1} and r_{vDC2} denote the dc-link voltage ripple ratios of SM_1 and SM_2; C_{11} and C_{21} denote the capacitance of qZS-network capacitor C_1 in SM_1 and SM_2, respectively. It can be seen that one SM's qZS-network capacitance varying is dominant on the dc-link voltage ripple of that SM, for instance, variations of C_{11} have large effects on r_{vDC1}, but little effects on r_{vDC2}; and r_{vDC2} is more largely affected when both C_{11} and C_{21} vary than only C_{11} varies. In all cases, all the ripples are less than 1% even at the $\pm 50\%$ parameter variations.

In an case, the tolerance of commercial inductors is usually within $\pm 20\%$, and that of commercial capacitors is within $\pm 25\%$. Usually a margin is adopted when selecting the passive components in practice. Then, as long as the inductance and capacitance are within the tolerance, the effects caused by circuit parameters mismatch are very little on the proposed control.

V. CONCLUSION

This article proposed a duty-cycle predictive control method for dc grid integration of qZS-MCC PV power system. The discrete-time circuit models of grid-connected current, qZS-HB input current, and qZS-network capacitor voltage were derived. Based on that, the active-state duty cycles and shoot-through duty cycles of the qZS-MCC SMs were predicted for the modulator to achieve the global grid-connected current control and each SM's dc-link voltage balancing control. The controller design and implementation of the proposed method got much simplified, resulting into less design effort needed than the conventional methods, due to no need of compensator parameters or weighting factors in the predictive control loop. Comparison results showed good steady-state stability, fast dynamic responses, and high robustness of the system using proposed method, compared with the PI-based control. The potential limitation of the proposed method would be to employ a PI regulator in the MPPT control of each submodule. Future work will be conducted on eliminating the PI regulator, i.e., achieving full predictive control of the system.

REFERENCES

[1] H. You and X. Cai, "Stepped 2-Level operation of three-port modular DC/DC converter applied in HVDC application," *IEEE Access*, vol. 6, pp. 53822–53832, 2018.
[2] F. Yan, P. Wang, X.-P. Zhang, J. Xie, X. Li, C. Tang, and Z. Zhao, "Coordinated start-up control and inter-converter oscillations damping for MMC-HVDC grid," *IEEE Access*, vol. 7, pp. 65093–65102, 2019.
[3] B. Li, Z. Xu, J. Ding, and D. Xu, "Fault-tolerant control of medium-voltage modular multilevel converters with minimum performance degradation under submodule failures," *IEEE Access*, vol. 6, pp. 11772–11781, 2018.
[4] X. Shi, B. Liu, Z. Wang, Y. Li, L. M. Tolbert, and F. Wang, "Modeling, control design, and analysis of a startup scheme for modular multilevel converters," *IEEE Trans. Ind. Electron.*, vol. 62, no. 11, pp. 7009–7024, Nov. 2015.
[5] J. I. Leon, S. Vazquez, and L. G. Franquelo, "Multilevel converters: Control and modulation techniques for their operation and industrial applications," *Proc. IEEE*, vol. 105, no. 11, pp. 2066–2081, Nov. 2017.

[6] C. A. Rojas, S. Kouro, M. A. Perez, and J. Echeverria, "DC–DC MMC for HVdc grid interface of utility-scale photovoltaic conversion systems," *IEEE Trans. Ind. Electron.*, vol. 65, no. 1, pp. 352–362, Jan. 2018.

[7] R. Li and F. Shi, "Control and optimization of residential photovoltaic power generation system with high efficiency isolated bidirectional DC–DC converter," *IEEE Access*, vol. 7, pp. 116107–116122, 2019.

[8] Y. Zhuang, F. Liu, Y. Huang, X. Zhang, and X. Zha, "A voltage-balancer-based cascaded DC–DC converter with a novel power feedforward control for the medium-voltage DC grid interface of photovoltaic systems," *IEEE Access*, vol. 7, pp. 178094–178107, 2019.

[9] Y. Liu, H. Abu-Rub, and B. Ge, "Front-end isolated quasi-Z-source DC-DC converter modules in series for photovoltaic high-voltage DC applications," in *Proc. IEEE Appl. Power Electron. Conf. Expo. (APEC)*, Mar. 2016, pp. 1214–1219.

[10] Y. Liu, H. Abu-Rub, and B. Ge, "Quasi-Z-source modular cascaded converter for high-power photovoltaic system," in *Proc. IEEE Int. Conf. Ind. Technol. (ICIT)*, Mar. 2016, pp. 1226–1231.

[11] Y. Liu, H. Abu-Rub, and B. Ge, "Front-end isolated quasi-Z-source DC–DC converter modules in series for high-power photovoltaic systems—Part I: Configuration, operation, and evaluation," *IEEE Trans. Ind. Electron.*, vol. 64, no. 1, pp. 347–358, Jan. 2017.

[12] Y. Liu, H. Abu-Rub, and B. Ge, "Front-end isolated quasi-Z-source DC–DC converter modules in series for high-power photovoltaic systems—Part II: Control, dynamic model, and downscaled verification," *IEEE Trans. Ind. Electron.*, vol. 64, no. 1, pp. 359–368, Jan. 2017.

[13] J. Anderson and F. Z. Peng, "Four quasi-Z-source inverters," in *Proc. 39th IEEE Annu. Power Electron. Spec. Conf. (PESC)*, Rhodes, Greece, Jun. 2008, pp. 2743–2749.

[14] Y. Liu, H. Abu-Rub, B. Ge, F. Blaabjerg, O. Ellabban, and P. C. Loh, *Impedance Source Power Electronic Converters*. Hoboken, NJ, USA: Wiley, Oct. 2016.

[15] K. Wolski, M. Zdanowski, and J. Rabkowski, "High-frequency SiC-based inverters with input stages based on quasi-Z-source and boost topologies—Experimental comparison," *IEEE Trans. Power Electron.*, vol. 34, no. 10, pp. 9471–9478, Oct. 2019.

[16] M. Uno and T. Shinohara, "Module-integrated converter based on cascaded quasi-Z-source inverter with differential power processing capability for photovoltaic panels under partial shading," *IEEE Trans. Power Electron.*, vol. 34, no. 12, pp. 11553–11565, Dec. 2019.

[17] Y. P. Siwakoti, F. Z. Peng, F. Blaabjerg, P. C. Loh, and G. E. Town, "Impedance-source networks for electric power conversion part I: A topological review," *IEEE Trans. Power Electron.*, vol. 30, no. 2, pp. 699–716, Feb. 2015.

[18] Y. P. Siwakoti, F. Z. Peng, F. Blaabjerg, P. C. Loh, G. E. Town, and S. Yang, "Impedance-source networks for electric power conversion part II: Review of control and modulation techniques," *IEEE Trans. Power Electron.*, vol. 30, no. 4, pp. 1887–1906, Apr. 2015.

[19] H. Choi, M. Ciobotaru, and V. G. Agelidis, "Cascaded H-bridge converter with multiphase isolated DC/DC converter for large-scale PV system," in *Proc. IEEE Int. Conf. Ind. Technol. (ICIT)*, Feb. 2014, pp. 455–461.

[20] O. Husev, L. Liivik, F. Blaabjerg, A. Chub, D. Vinnikov, and I. Roasto, "Galvanically isolated quasi-Z-source DC–DC converter with a novel ZVS and ZCS technique," *IEEE Trans. Ind. Electron.*, vol. 62, no. 12, pp. 7547–7556, Dec. 2015.

[21] S. A. Gorji, H. G. Sahebi, M. Ektesabi, and A. B. Rad, "Topologies and control schemes of bidirectional DC–DC power converters: An overview," *IEEE Access*, vol. 7, pp. 117997–118019, 2019.

[22] O. Ellabban, J. Van Mierlo, and P. Lataire, "A DSP-based dual-loop peak DC-link voltage control strategy of the Z-source inverter," *IEEE Trans. Power Electron.*, vol. 27, no. 9, pp. 4088–4097, Sep. 2012.

[23] M. K. Kazimierczuk, "Small-signal modeling of open-loop PWM Z-source converter by circuit-averaging technique," *IEEE Trans. Power Electron.*, vol. 28, no. 3, pp. 1286–1296, Mar. 2013.

[24] B. Ge, H. Abu-Rub, F. Z. Peng, Q. Lei, A. T. de Almeida, F. J. T. E. Ferreira, D. Sun, and Y. Liu, "An energy-stored quasi-Z-source inverter for application to photovoltaic power system," *IEEE Trans. Ind. Electron.*, vol. 60, no. 10, pp. 4468–4481, Oct. 2013.

[25] A. Lashab, D. Sera, J. Martins, and J. M. Guerrero, "Dual-input quasi-Z-source PV inverter: Dynamic modeling, design, and control," *IEEE Trans. Ind. Electron.*, vol. 67, no. 8, pp. 6483–6493, Aug. 2020.

[26] S. Hu, Z. Liang, and X. He, "Research on the dynamic characteristics and regulation method of the energy stored Quasi-Z-Source inverter system," *IEEE Trans. Ind. Electron.*, vol. 67, no. 6, pp. 4590–4599, Jun. 2020.

[27] J. I. Leon, S. Kouro, L. G. Franquelo, J. Rodriguez, and B. Wu, "The essential role and the continuous evolution of modulation techniques for voltage-source inverters in the past, present, and future power electronics," *IEEE Trans. Ind. Electron.*, vol. 63, no. 5, pp. 2688–2701, May 2016.

[28] D. Sri Vidhya and T. Venkatesan, "Quasi-Z-source indirect matrix converter fed induction motor drive for flow control of dye in paper mill," *IEEE Trans. Power Electron.*, vol. 33, no. 2, pp. 1476–1486, Feb. 2018.

[29] H. Rostami and D. A. Khaburi, "Neural networks controlling for both the DC boost and AC output voltage of Z-source inverter," in *Proc. 1st Power Electron. Drive Syst. Technol. Conf. (PEDSTC)*, Feb. 2010, pp. 135–140.

[30] J. Liu, S. Jiang, D. Cao, and F. Z. Peng, "A digital current control of quasi-Z-source inverter with battery," *IEEE Trans. Ind. Informat.*, vol. 9, no. 2, pp. 928–937, May 2013.

[31] U. K. Shinde, S. G. Kadwane, S. P. Gawande, M. J. B. Reddy, and D. K. Mohanta, "Sliding mode control of single-phase grid-connected quasi-Z-source inverter," *IEEE Access*, vol. 5, pp. 10232–10240, 2017.

[32] S. Bayhan and H. Komurcugil, "A sliding-mode controlled single-phase grid-connected quasi-Z-source NPC inverter with double-line frequency ripple suppression," *IEEE Access*, vol. 7, pp. 160004–160016, 2019.

[33] F. Bagheri, H. Komurcugil, O. Kukrer, N. Guler, and S. Bayhan, "Multi-input Multi-Output-Based sliding-mode controller for single-phase quasi-Z-source inverters," *IEEE Trans. Ind. Electron.*, vol. 67, no. 8, pp. 6439–6449, Aug. 2020.

[34] A. Bakeer, M. A. Ismeil, and M. Orabi, "A powerful finite control set-model predictive control algorithm for quasi Z-source inverter," *IEEE Trans. Ind. Informat.*, vol. 12, no. 4, pp. 1371–1379, Aug. 2016.

[35] S. Bayhan, M. Trabelsi, H. Abu-Rub, and M. Malinowski, "Finite-control-set model-predictive control for a Quasi-Z-Source four-leg inverter under unbalanced load condition," *IEEE Trans. Ind. Electron.*, vol. 64, no. 4, pp. 2560–2569, Apr. 2017.

[36] M. Mosa, R. S. Balog, and H. Abu-Rub, "High-performance predictive control of quasi-impedance source inverter," *IEEE Trans. Power Electron.*, vol. 32, no. 4, pp. 3251–3262, Apr. 2017.

[37] H. Mahmoudi, M. Aleenejad, and R. Ahmadi, "Modulated model predictive control for a Z-source-based permanent magnet synchronous motor drive system," *IEEE Trans. Ind. Electron.*, vol. 65, no. 10, pp. 8307–8319, Oct. 2018.

[38] S. Sajadian and R. Ahmadi, "Model predictive control of dual-mode operations Z-source inverter: Islanded and grid-connected," *IEEE Trans. Power Electron.*, vol. 33, no. 5, pp. 4488–4497, May 2018.

[39] P. Karamanakos, A. Ayad, and R. Kennel, "A variable switching point predictive current control strategy for quasi-Z-source inverters," *IEEE Trans. Ind. Appl.*, vol. 54, no. 2, pp. 1469–1480, Mar./Apr. 2018.

[40] D. Xu, J. Liu, X.-G. Yan, and W. Yan, "A novel adaptive neural network constrained control for a multi-area interconnected power system with hybrid energy storage," *IEEE Trans. Ind. Electron.*, vol. 65, no. 8, pp. 6625–6634, Aug. 2018.

[41] Y. Yin, J. Liu, J. A. Sanchez, L. Wu, S. Vazquez, J. I. Leon, and L. G. Franquelo, "Observer-based adaptive sliding mode control of NPC converters: An RBF neural network approach," *IEEE Trans. Power Electron.*, vol. 34, no. 4, pp. 3831–3841, Apr. 2019.

[42] Q. Wei, B. Wu, D. Xu, and N. R. Zargari, "Model predictive control of capacitor voltage balancing for cascaded modular DC–DC converters," *IEEE Trans. Power Electron.*, vol. 32, no. 1, pp. 752–761, Jan. 2017.

[43] Y. Liu, H. Abu-Rub, Y. Xue, and F. Tao, "A discrete-time average model-based predictive control for a quasi-Z-source inverter," *IEEE Trans. Ind. Electron.*, vol. 65, no. 8, pp. 6044–6054, Aug. 2018.

[44] L. Malesani, P. Mattavelli, and S. Buso, "Robust dead-beat current control for PWM rectifiers and active filters," *IEEE Trans. Ind. Appl.*, vol. 35, no. 3, pp. 613–620, May/Jun. 1999.

[45] B. Ge, Y. Liu, H. Abu-Rub, R. S. Balog, F. Z. Peng, S. McConnell, and X. Li, "Current ripple damping control to minimize impedance network for single-phase quasi-Z source inverter system," *IEEE Trans. Ind. Informat.*, vol. 12, no. 3, pp. 1043–1054, Jun. 2016.

[46] W. Liang, Y. Liu, B. Ge, H. Abu-Rub, R. S. Balog, and Y. Xue, "Double-line-frequency ripple model, analysis, and impedance design for energy-stored single-phase quasi-Z-source photovoltaic system," *IEEE Trans. Ind. Electron.*, vol. 65, no. 4, pp. 3198–3209, Apr. 2018.

YINGJUN GUO received the master's degree from the Beijing Institute of Technology, China, in 2004. He is currently pursuing the Ph.D. degree in control theory and control engineering with the Hebei University of Technology. He is also an Associate Professor with the Hebei University of Science and Technology. His research interests include wind power control and power electronic devices.

HEXU SUN (Senior Member, IEEE) received the Ph.D. degree in automation from Northeastern University, Shenyang, China, in 1993. He has been a Professor with the School of Control Science and Engineering, Hebei University of Technology, Tianjin, China, and the School of Electrical Engineering, Hebei University of Science and Technology, Shijiazhuang, China. He has authored five books and more than 130 journal and conference papers, and holds 13 U.S. patents and five computer software copyrights. His current research interests include robotics and complex engineering systems. He was a recipient of many prestigious national awards from China. He was the Director of many societies and committees in China. He is currently the Invited Plenary Speaker and the General Co-Chair of many international conferences.

YI ZHANG received the master's degree from the Hebei University of Technology, China, in 2005, where he is currently pursuing the Ph.D. degree in control theory and control engineering. He is currently a Lecturer with the School of Information Science and Engineering, Hebei University of Science and Technology. His research interests include wind power prediction and the application of machine learning in the wind energy.

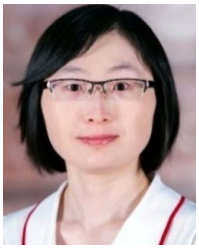

YUSHAN LIU (Senior Member, IEEE) received the B.Sc. degree in automation from the Beijing Institute of Technology, Beijing, China, in 2008, and the Ph.D. degree in electrical engineering from the School of Electrical Engineering, Beijing Jiaotong University, Beijing, in 2014.

She was a Postdoctoral Fellow and the Assistant Research Scientist of the Department of Electrical and Computer Engineering, Texas A&M University at Qatar, Doha, Qatar, from 2014 to 2017. She is currently an Associate Professor with the School of Automation Science and Electrical Engineering, Beihang University, Beijing. She has published more than 70 journal and conference papers, one book, and one book chapter in the area of expertise. Her research interests include impedance source inverters, cascade multilevel converters, photovoltaic power integration, renewable energy systems, model predictive control, and smart transformers.

Dr. Liu received the ''Research Fellow Excellence Award'' from Texas A&M University at Qatar, the ''Excellent Doctoral Dissertations'' Prize from Beijing Jiaotong University. She is also an Associate Editor of the IEEE TRANSACTIONS ON INDUSTRIAL ELECTRONICS and the IEEE OPEN JOURNAL OF THE INDUSTRIAL ELECTRONICS SOCIETY.

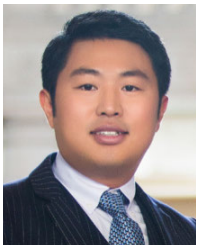

XIAO LI (Member, IEEE) received the B.Sc. degree in automation from the Harbin Institute of Technology (HIT), China, in 2012, and the Ph.D. degree in electrical engineering from the Department of Electrical and Computer Engineering, Texas A&M University, College Station, TX, USA.

His research interests include power electronics system integration, distributed generations, general power electronic circuit topologies, modeling and control, and wide bandgap devices.

YAOSUO XUE (Senior Member, IEEE) received the B.Sc. degree in electrical engineering from East China Jiaotong University, Nanchang, China, in 1991, and the M.Sc. degree in electrical engineering from the University of New Brunswick, Fredericton, Canada, in 2004.

From 1991 to 2000, he was an Electrical Engineer-in-Charge with China Railway Design Corporation and led the traction power systems Research and Development of the first China's high-speed railway. From 2005 to 2006, he has worked with Capstone Turbine Corporation as a Lead Power Electronics and Systems Engineer. From 2006 to 2008, he was a NSERC PGS-Doctor Scholar with the University of New Brunswick. He was with Siemens Corporate Research, from 2009 to 2015, and established the Corporate Technology USA Power Electronics Program. He is currently with the Oak Ridge National Laboratory. His research interests include multilevel converters and smart inverter controls for renewable energy and utility applications.

He is an Associate Editor of the IEEE TRANSACTIONS ON POWER ELECTRONICS and the IEEE JOURNAL OF EMERGING AND SELECTED TOPICS IN POWER ELECTRONICS.